Design and Testing of a Large-Aperture, High-Gain, Brewster's-Angle, Zig-Zag Nd:Glass Slab Amplifier

The slab-geometry amplifier was invented in 1969 by Chernoch and Martin.[1] The advantages of the slab geometry have been enumerated by many authors[2] and will not be repeated here. A resurgence of interest occurred in 1982 as a result of work at Stanford University[3] on sources for remote sensing. Improvements in actual devices and theoretical understanding continued there[4,5] and elsewhere.[6,7]

The University of Rochester's Laboratory for Laser Energetics (LLE) began design and construction of a slab-geometry system specifically for use as a source for materials testing. This device incorporates, in one unit, many of the incremental improvements reported previously, including improved cooling, uniform pumping, high stored-energy density, simplified amplified spontaneous emission (ASE) suppression, and improved wavefront. One goal in the design was to avoid, wherever possible, the use of complex propagation codes, relying instead on careful design choices guided by physical insight obtained from analytic calculations and previous work. This article presents the resulting design and describes its measured performance.

The amplifier is made of Nd-doped LHG-5 phosphate laser glass[8] with physical dimensions of $31.0 \times 8.0 \times 1.1$ cm and a doping of 3.3 wt% Nd_2O_3. The ends of the slab are parallel cut at Brewster's angle. The clear aperture, defined as the unobstructed part of the aperture, is 1.0×6.6 cm and has a single-pass, small-signal gain of 8 and a 2-Hz maximum repetition rate.

Design

The amplifier is used in a facility where optical materials are tested for use in fusion-driver Nd lasers. The wavelengths of interest are the fundamental and the first two harmonics. The pulse widths of interest are 0.1- to 1.1-ns FWHM. The energy required is 4 J at 1 ns decreasing to ~1.3 J at 0.1 ns, limited by downstream optical coatings. The slab driver is capable of producing ~10 mJ of energy at 1 ns, thus requiring a slab-stage gain of ~400. The data acquisition in this facility requires the processing of images and is consequently limited to <2 Hz. The maximum design repetition rate of the slab was therefore set to 2 Hz.

1. Optical Design

The terminology for the various slab surfaces is shown in Fig. 68.42. In addition to these surfaces and the edges, three regions of the slab are referred to specifically. The side regions of the slab are the two pumped areas of the slab within one-half slab thickness of the sides, where propagation is disturbed by strain relief from the sides. The transition regions are the two areas of the slab near the ends, where a transition from pumped to unpumped glass is made. Finally, the central region of the slab is where the glass is uniformly pumped and the surface displacements are essentially uniform. Each of these regions is handled separately in the optical design to ensure wavefront quality.

High stored-energy densities are desirable in high-peak-power systems to avoid deleterious nonlinear effects such as self-focusing.[9] Typical thickness-averaged stored-energy densities (E_s) achieved in other large phosphate-glass, plate-geometry lasers were in the range of 0.3 to 0.33 J/cm^3.[10] These were achieved with single-sided pumping at a flash-lamp explosion fraction (f_x) of 0.34. Slab amplifiers can be double sided pumped with flash lamps derated to $f_x = 0.20$ for average-power handling. A simple scaling (ignoring ASE and thickness effects) suggested a stored-energy density near 0.50 J/cm^3. An E_s of 0.45 J/cm^3 was chosen as a conservative goal.

Over the pulse-width range of interest (~1 ns), the aperture required for one pass of the amplified beam—the beam clear aperture—is determined by the most-damage-threatened component after the slab. This is a graded-index[11] antireflection coating on the input lens to a spatial filter with a damage fluence approximated by[12]

$$\text{damage fluence}\left(\text{J/cm}^2\right) = 12\ \tau^{0.5}, \qquad (1)$$

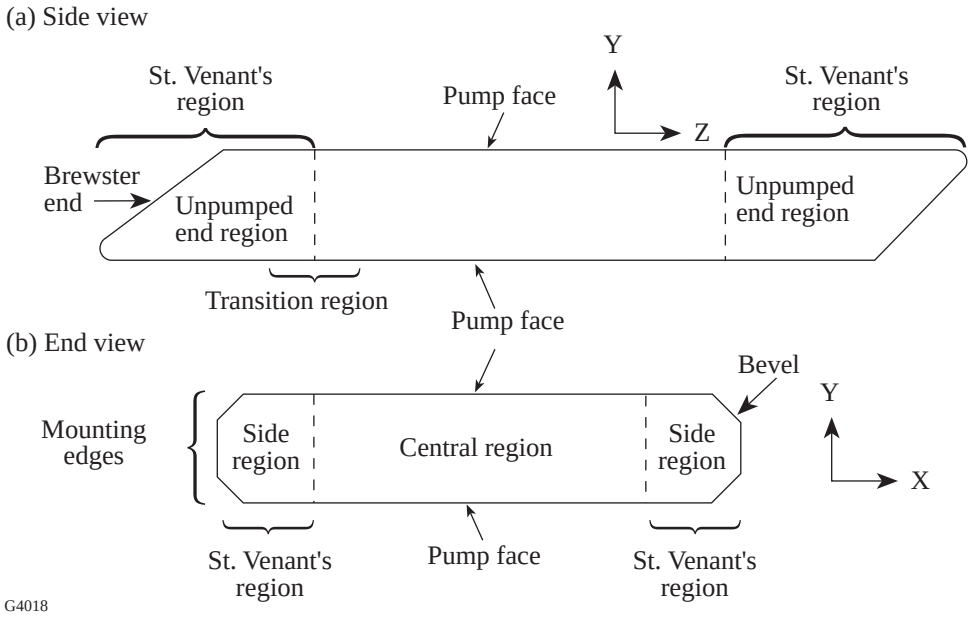

Figure 68.42
Orthogonal cross-sectional views of a face-pumped slab showing key features.

where τ is the pulse FWHM in nanoseconds. A TEM_{00} beam drives the slab with 1% intensity points assumed to be at the edge of the clear aperture. The on-axis fluence of this beam is six times the average fluence calculated by the energy divided by the clear aperture. A further safety factor of 1.8 is assumed[13] to allow for modulation (due to diffraction from surface scratches, etc.) on the beam. The beam clear aperture (C.A.) at the exit face is thus

$$\text{C.A.} = \frac{4\,\text{J} \times 6 \times 1.8}{\left(12\ \text{J/cm}^2\right)} \geq 3.6\ \text{cm}^2. \tag{2}$$

Since it is desirable to multiplex more than one pass through the slab, the *total* clear aperture is twice this or 6.5 cm^2.

Assuming a uniform[14] deposition of the pump light through the thickness (see Fig. 68.42) of the slab and equal cooling on both faces, the maximum stress σ_s in a slab of infinite extent occurs on the surface and is given by[4]

$$\sigma_s = \frac{Q}{12\ M_s} t^2, \tag{3}$$

where Q is the heat power per unit volume, t is the thickness, and M_s is the material figure of merit. The material figure of merit is defined as

$$M_s = \left[\frac{(1-\nu)k}{\alpha E}\right], \tag{4}$$

where ν is Poisson's ratio, α is the coefficient of linear expansion, k is the thermal conductivity, and E is Young's modulus. Because the size of defects at which fracture initiates is unknown, it is desirable to operate at some fraction b of the reported fracture stress σ_f for long slab life. Typical b values are ~0.2.[2] Equating and rearrangement yield

$$t^2 = \sigma_f M_s \frac{2.4}{Q}. \tag{5}$$

The quantity $\sigma_f M_s$ is known as the thermal shock parameter R_s of the material and is tabulated.[15] Q is given by

$$Q = E_s\, \chi f, \tag{6}$$

where f is the repetition rate and χ is the normalized heating parameter[16] defined as the ratio of heat energy to peak stored-energy density (E_s). Substituting and solving for t:

$$t = \left[R_s \frac{2.4}{E_s \chi f}\right]^{1/2}. \tag{7}$$

For a stored energy of 0.45 J/cm^3, an R_s = 1 W/cm,[15] and χ of 2.2,[16] the maximum slab thickness is 1.10 cm. The clear aperture in the thickness direction is slightly smaller to allow for the fact that the slab tip must be radiused slightly (~0.25 mm) to avoid damage during manufacture and handling. The actual clear aperture in this dimension is 0.92 cm. The extracting beam is therefore elliptical, with an aspect ratio (width to thickness) of 3.6:1.

The width of the clear aperture is 6.6 cm, and the physical width of the slab may now be calculated since the slab thickness is also known. The physical width of the slab must be wider by at least one slab thickness (one-half St. Venant's region at each side) to avoid the distorted major faces and depolarized region caused by stress relief [5] at the free sides. The physical width of this slab is 8.0 cm.

The pumped length of the slab is determined approximately by the gain requirement. Assuming a propagation angle θ of 20° (see Fig. 68.43), the *z*-direction length required for a small-signal gain of 8 is given by

$$L = \frac{\ln(8)\cos(\theta)}{\alpha_0 E_s} = 20.0 \text{ cm}, \tag{8}$$

where α_0 is the specific gain coefficient of the glass. The exact length of the pumped region is adjusted to align the pumped-to-unpumped transition regions to minimize wavefront errors across the narrow dimension of the beam. The physical length of the slab is longer than the pumped length to reduce stress-induced deformation of the entrance and exit ends of the slab. It is desirable to locate the center of each end at least one-half St. Venant's distance from the pumped region. The St. Venant's distance may be defined as the slab thickness (see Fig. 68.42), which is relevant for bending the end in the *y*-direction, or as the slab width that is relevant for bending the end in the *x*-direction. An additional 4 cm was added at each end.

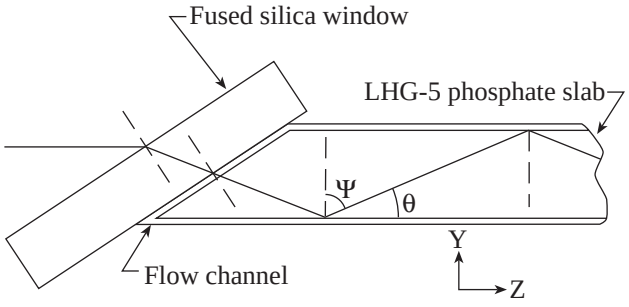

Figure 68.43
Entering or exiting ray for a Brewster's-angle slab with Brewster face cooling.

The exact physical length of the slab is set to ensure an even number of total-internal-reflection (TIR) bounces in the slab. To calculate the number of bounces *N*, the exact propagation angle θ must be known. The angle θ is the complement of Ψ, which was chosen for entrance to the slab near Brewster's angle for low loss and high internal fill. For this slab, Ψ = 66.91°, the slightly larger value chosen to allow for coolant mixtures with greater than 50% ethylene glycol (n = 1.424 at λ = 1054 nm)[17] and/or the future addition of evanescent-wave coatings.[18] The minimum slab length is the 20.0-cm pumped length plus both of the 4.0-cm runout regions at the ends. This corresponds to 10.85 bounces, so the next largest even number of bounces is chosen (12) for a slab length of 30.966 cm.

The entire slab, including the Brewster ends, is immersed in coolant. This strategy further reduces end-deformation effects on the beam. The optical power ϕ of the deformed end is proportional to

$$\phi = \frac{-c}{(n/n')}, \tag{9}$$

where c is the local curvature of the interface and n/n' is the ratio of the initial to final refractive indices. Immersing the end in coolant ($n_{1054\text{ nm}}$ = 1.375) reduces the optical power by a factor of the refractive index of the coolant. This strategy also eliminates the need for liquid seals to the slab, which must simultaneously withstand flash-lamp radiation, not distort the slab, and not leak. Enclosing the ends also protects them mechanically. Coolant flow over the entire unpumped region of the slab's faces maintains good thermal control in that region. Finally, it has been our experience that the liquid flow continuously cleans the Brewster ends, thereby removing the maximum damage threat from the expensive slab to the less-expensive entrance/exit windows. Figure 68.43 is a detail of the end treatment. The coolant thickness must be chosen to ensure sufficient flow to guarantee a complete coolant replacement between shots and simultaneously minimize absorption (α_c = 0.188 cm^{-1} at 1054 nm).[17] There is less than 1.64% absorption in the 1-mm coolant channel shown in Fig. 68.43.

The pumped length of the slab is adjusted to ensure that the ray-integrated optical path through both pumped-to-unpumped

transition regions does not vary with ray position in the extracting beam.[19] This ensures that piston-like phase defects along any ray sum to a constant value. The major concern here is OPD variation in the narrow dimension of the beam. These variations can arise from three sources: reflection from a displaced pump face, the variation of refractive index with stress (stress-optic effect), and the variation of refractive index with temperature. The last effect is of no concern since $dn/dT \sim 0.0$[20] for LHG-5 glass used here.

Displacements of the face over the area of the beam imprint occur in the transition regions from pumped-to-unpumped glass and may be calculated by integrating the strain field perpendicular to the pump face. The strain field is calculated from the thermal-source function $Q(x, y, z)$ using a finite-element code and the thermal boundary conditions. A Monte Carlo code[21] tracing ~1/2 million rays at 200 wavelengths from the flash lamps into the glass volume calculates the thermal source function. Temperature contours plotted within a longitudinal cross section of the slab are shown in Fig. 68.44. Not shown in Fig. 68.44 is the central region of the slab where the surface displacements are uniform across a beam footprint. The pumped length has been adjusted to 22.3 cm so that a ray at the entrance transition region TIRing from a portion of the face with a large displacement, TIR's from a portion of the face in the exit transition region that suffers only a small displacement. The length of the pumped region has been adjusted such that the sum of the pump face displacements sampled by the beam in the entrance and exit transition regions approximates a constant.

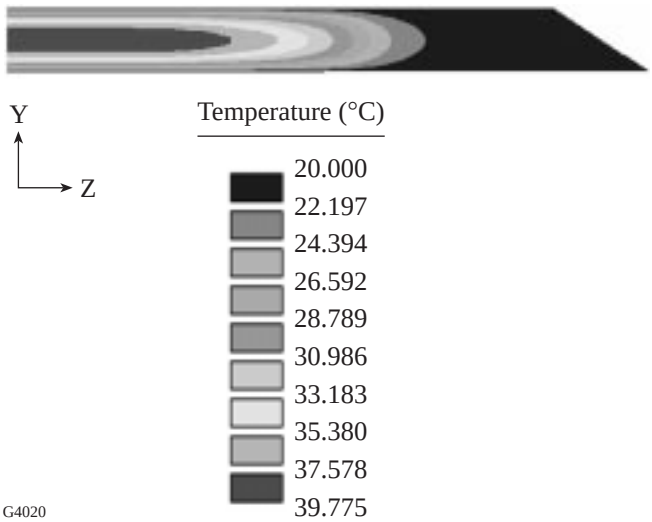

Figure 68.44
Longitudinal cross-sectional view showing the thermal distribution in the transition region.

The total change in pump face displacement over the length of a single beam footprint is minimized by making the transition region gradual. In this device the transition region is made less abrupt by locating the long-direction (end) reflectors well behind the electrodes of the flash lamps, thus rolling off the illumination in the *z*-direction before the slab goes under the end reflector.

The final aspect of the optical design is ensuring the uniformity of the central pumped region of the slab. Both the pumping and the cooling in this region must be as uniform as possible. The cooling is described in the following thermal design section. Early in the design, the transverse orientation [lamp axis parallel to width (*x*-axis shown in Fig. 68.42) of the slab] of the flash lamps was rejected because it could guarantee neither transverse nor longitudinal uniformity of pumping. Transverse uniformity requires that the lightly loaded (low-f_x) flash lamps be long compared to the width of the slab. To ensure adequate plasma opacity at the side of the slab, each electrode should be located at least two lamp diameters beyond the side of the slab. Any nonuniformities in the longitudinal direction due to the transverse lamps cannot be ameliorated by the compensation technique described previously because it is extremely unlikely that the lamp spacing for maximum uniformity will be the same as one bounce length.

Longitudinal orientation of the lamps guarantees *z*-direction uniformity as long as the arc fills the bore of the lamp and the aspect ratio (length to bore) of the lamps is sufficiently large. Filling the bore may be improved by prepulsing[22] the lamps. The reduced efficiency of emission from the lamp near the electrodes may be used to advantage to grade the pumped-to-unpumped transition region. The design goal reduces then to delivering sufficient energy, uniformly in the transverse direction.

The total stored energy in the slab at 0.45 J/cm^3 is 85 J. At a nominal storage efficiency (stored energy divided by energy stored in flash-lamp capacitors) of 1.5%, 5.7 kJ must be delivered to the flash lamps. A pump pulse width measured at 1/3 current max points of 350 μs is used, 25% longer than the ~280-μs fluorescent lifetime of the slab. At an explosion fraction f_x of 20% the minimum required arc length may be calculated from[23]

$$L = \frac{E_0}{17000\ f_x d(T/3)^{1/2}} = 80.25\ \text{cm}, \qquad (10)$$

where $d = 1.9$ cm is the lamp bore, E_0 is the energy delivered to the lamps, and T is the pump pulse width measured at the 1/3 current max points. The calculated total flash-lamp arc length required in this case is just under 32 in. Since flash lamps are conventionally ordered in integer inch lengths, the arc length was chosen to be 8 in. with two lamps pumping each side of the slab. One pulse-forming network drives a series-connected pair of lamps. Size-*E* ignitrons are used as switches instead of SCR's due to the high peak currents and large coulomb transfer.

Figure 68.45 shows a basic schematic of the pump cavity with all components listed. Within the pump cavity are several components that can be optimized for size, position, or type of reflective surface. To evaluate the uniformity of this cavity, the Monte Carlo ray-trace code ZAP[21] was used. Average *S*- and *P*-polarization properties were used. Measured or calculated reflection/refraction properties were assigned to surfaces in the cavity. Similarly, measured or calculated absorption/emission properties were assigned to volumes within the model. ZAP had been previously normalized to two other slab amplifiers. The approach to optimizing the pump geometry had two goals: (1) keep the cavity as simple as possible for fabrication reasons, and (2) keep the number of components in the cavity to a minimum. Reflector optimizations were performed for both a specular and a diffuse pump cavity. All simulations were time instantaneous at the peak of the flash-lamp pulse. Simulations done at other times during the flash-lamp pulse showed negligible change in the deposition profile. Reabsorption by the flash-lamp plasma was accounted for but none of the reabsorbed energy was reemitted. This was an excellent approximation because even at peak current density in the lamps, only 17% of the flash lamp's emitted light was reabsorbed.

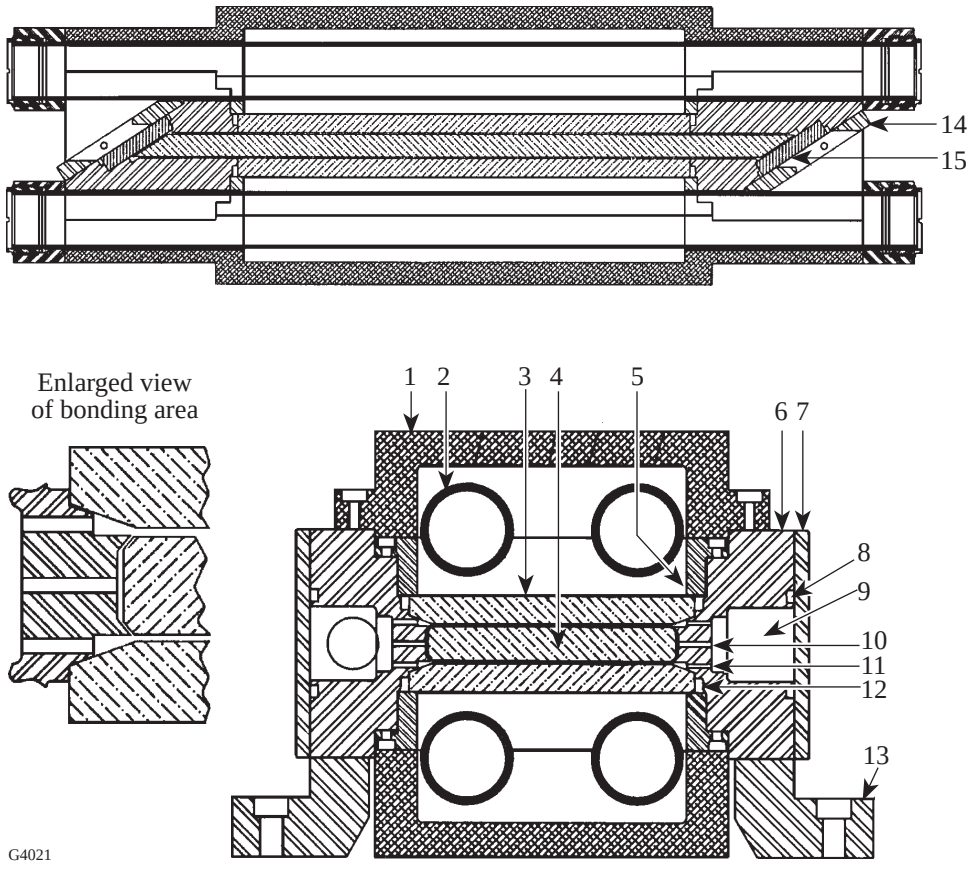

1. Reflector
2. Water jacket
3. Pump window
4. LHG-5 slab
5. Retainer
6. Frame
7. Side plate
8. Side plate o-ring groove
9. Plenum
10. Glue injection hole
11. Flow hole
12. Pump window o-ring groove
13. Support leg
14. Endcap
15. Brewster window

Figure 68.45
Orthogonal cross sections of the slab amplifier detailing all components.

After numerous simulations, some general statements regarding rectangular pump cavities could be made. The uniformity was fairly insensitive to changes in the shape of the pump cavity. In particular, angling the side of the reflector cavity up to 20° showed little or no improvement in uniformity or efficiency. Changing the roof of the cavity or adding a center reflector also showed little or no improvement in pump uniformity. The pump window retainer, however, showed substantial improvement in transfer and uniformity when specular and not diffuse. This is intuitively obvious since a diffuse surface would tend to send a fraction of the light back toward the lamps. Uniformity improvements were seen at the edges of the slab, which allowed the lamps to be moved toward the center of the slab.

The reflector materials were chosen simply on a cost basis. The specular reflectors are 6061-T6 aluminum polished to a 0.10-μm finish and then plated with 0.0127 to 0.0152 mm of electroless nickel. The nickel was then coated with *e*-beam-deposited silver. To prevent the silver from tarnishing, a silicon dioxide overcoat was applied.

Two sets of diffuse reflectors were designed: one metallic, the other ceramic. The metallic reflectors are the same as the specular except, instead of a polished surface, the surface is beadblasted with a fine bead size until all machining marks are removed. The reflectors are then plated in the same manner as the specular reflectors. The ceramic reflectors were fabricated from Macor®.[24,25]

2. Cooling

The cooling design of the slab requires uniform heat removal from the pump faces as well as tolerance to variations in the cooling-channel height. The temperature rise across the pump face is also minimized to reduce dn/dT effects across the aperture. With the pump volume, stored-energy density (E_s), and maximum repetition rate (f) known, the maximum average power loading P_a is given as

$$P_a = f\, V_p\, E_s \chi . \tag{11}$$

For steady-state conditions, all of the deposited thermal power is removed by the coolant. The thermal power deposited in the slab results in a temperature rise in the coolant. The energy balance equation can be written as

$$Q = \dot{m} c_p \left(T_o - T_i\right), \tag{12}$$

where Q is deposited thermal power, $\dot{m}$ is the coolant mass flow rate, T_o is exiting coolant temperature, and T_i is the entering coolant temperature. A coolant temperature rise of 0.1°C is the design point. From this, the required mass-flow rate over the pump region is calculated as a function of power loading and ΔT. $\dot{m}$ is the minimum mass-flow rate required to remove the deposited heat from the slab. This mass-flow rate may be sufficient to remove the heat load; however, it may be insufficient to establish turbulent flow in the coolant channel. To maximize the heat-transfer capabilities of the coolant it is desirable to operate in the turbulent regime. If this condition exists, then the minimum mass-flow rate to establish turbulent flow is calculated.

The slab is completely submersed in coolant. For now, only the portion of the coolant channel in the pump regions is considered. To account for the total coolant requirements, simply multiply by the ratio of total slab perimeter divided by twice the pumped length. The coolant channels are 20.65 × 0.076 cm. The two coolant channels flow in parallel, which must be accounted for in all calculations. From Eq. (12), the minimum mass-flow rate $(\dot{m})$ is 1088 gm/s.

We now calculate the Reynolds number (*Re*) to verify that the flow rate is in the turbulent regime. Turbulent flow is typically achieved for *Re* > 2300 although laminar flow for $Re = 10^5$ has been demonstrated for special cases. The Reynolds number, which is the ratio of the inertia and viscous forces, is defined as

$$Re = \frac{\rho D u}{\mu}, \tag{13}$$

where ρ is the coolant density, u is the fluid flow velocity, D is the hydraulic diameter, and μ is the dynamic viscosity of the coolant.

The hydraulic diameter D for a square channel can be written as

$$D = \frac{4A_c}{P}, \tag{14}$$

where A_c is the cross-sectional area of the coolant channel and P is the wetted perimeter of the coolant channel, which is $P = 2\left(l_p + t\right)$.

The fluid flow velocity u is defined as

$$u = \frac{4V}{PD} . \tag{15}$$

Substituting Eqs. (14) and (15) into Eq. (13) yields an expression for the Reynolds number as a function of mass-flow rate and wetted perimeter P:

$$Re = \frac{4\dot{m}}{\mu P} . \tag{16}$$

Since half of the previously calculated mass flow goes to each coolant channel, $\dot{m}/2$ is used. Equation (16) yields a Reynolds number of 1400, which is clearly laminar. Solving Eq. (16) with Re = 2300 yields a minimum $\dot{m}$ = 1792 gm/s for turbulent flow.

The local convective film coefficient h in the coolant channel is required for thermal modeling of the slab. The film coefficient may be determined from the Nusselt number (Nu):

$$h = \frac{k\ Nu}{D} , \tag{17}$$

where k is the thermal conductivity. The Nusselt number may be calculated using empirically determined correlations. For this calculation, the Petukhov[26] correlation was used:

$$Nu = \frac{RePrc_f/2}{1.07 + 12.7\left(Pr^{2/3} - 1\right)\left(c_f/2\right)^{1/2}} , \tag{18}$$

where c_f is the friction coefficient and is empirically[26] determined to be

$$\frac{c_f}{2} = \left[2.236 \ln(Re) - 4.639\right]^{-2}, \tag{19}$$

the Prandtl number Pr is defined to be

$$Pr = \frac{c_p \mu}{k} , \tag{20}$$

and c_p is the specific heat of the coolant.

The height of the coolant channel is an important parameter for a number of reasons. Since the channel height directly affects the hydraulic diameter, it also directly affects the flow velocity and the Reynolds and Nusselt numbers. The hydrodynamic entry length $x_{fd,h}$, which is the distance required to obtain a fully developed flow profile, is also affected. This is of importance since the convective film coefficient varies with the flow profile. Since no general expression for the entry length in turbulent flow exists, a first approximation is found using[27]

$$10 \le \frac{x_{fd,h}}{D} \le 60 . \tag{21}$$

It can then be concluded that either the hydraulic diameter must be minimized or a suitable entry length must be designed into the amplifier.

The effect of the channel height on the flow velocity can be readily seen in Eqs. (14) and (15). The net effect is simply an increase in the flow velocity with decreasing height. This may not seem to have any significant impact on the cooling dynamics of the amplifier; however, there is a significant impact in the area of pressure drops Δp. This is readily seen from

$$\Delta p = f\left(\frac{L}{D}\right)\frac{1}{2}\rho u^2, \tag{22}$$

where the pressure drop is proportional to the flow velocity squared, f is the friction factor, and L is the distance traversed. Pressure drops will be discussed later.

The effects on the Reynolds number are negligible at best. Since the coolant channel has a high aspect ratio $l_p >> t$, the effects of the channel height are negligible. From this, it is also obvious that the Reynolds number is also insensitive to variations of the channel height. From this and Eq. (14), it is shown that the effects on the Nusselt number are also negligible.

From Eq. (17), the importance of reducing the hydraulic diameter to increase the convective film coefficient is established. It is desirable to have a low hydraulic diameter; however, we are bounded by the pressure required to move the coolant through the channel. Equation (22) can be reduced to

$$\Delta p = \frac{f}{4} L\rho V^2 \frac{\left(l_p + t\right)}{\left(l_p t\right)^3} , \tag{23}$$

which shows the pressure dependence on the channel height where V is the volumetric flow rate. Equation (23) neglects any effects on the friction coefficient because it was previously stated that the effects on the Reynolds number were

negligible. The friction factor is defined in Table 68.V for various Reynolds numbers.

As a design goal we wanted to keep the pressure drop of the amplifier below 5 psi to prevent pressure-induced deformation of the input and output Brewster windows.

3. Linear Optical Effects in the Coolant Channel

In propagating through the coolant channel, dn/dT effects can cause significant wavefront errors. As a design point, we chose to keep this error less than $\lambda/10$. This error can be directly controlled by varying the propagation distance through the coolant channel. For a first-order approximation of the wavefront error, we assume instantaneous and uniform heating through the coolant channel. Assuming a peak fluence F_p of 10 J/cm^2 over a unit area of 1 cm^2 and using the linear absorption coefficient α of ethylene glycol and water, we calculate a temperature rise of 0.52°C using

$$\Delta T = \frac{Q}{mc_p}, \tag{24}$$

where $Q = a_c F_p$.

From this the optical-path-length difference is found using

$$\Delta d = \frac{dn}{dt}\,\Delta T d, \tag{25}$$

where d is the path length through the coolant channel. The value dn/dT was the average of water (-1.2×10^{-6}/°C)[17] and ethylene glycol (-2.7×10^{-6}/°C).[17] The resultant path-length difference was $\lambda/12$ at 1054 nm.

4. Nonlinear Optical Effects in the Coolant Channel

High-peak-power laser systems can be limited by a variety of nonlinear effects. The limitations imposed by these effects, which include self-focusing and stimulated scattering, are well understood for conventional materials such as fused silica and laser glass.[28] In this slab design, the high-peak-power beam propagates through the thin (0.088 cm, corrected for Brewster's angle) cooling channel's 50%/50% (by volume) mixture of flowing ethylene glycol and water.

The thinness of the channel (0.088 cm) would require a nonlinear index of the coolant to be two orders of magnitude greater than that of typical solids before self-focusing would be a problem, which is not likely. Similarly, the thinness reduces the gain-length product for forward and backward stimulated scattering to very small values. However, transverse stimulated scattering could experience significant gains. Since Raman gain coefficients are typically an order of magnitude lower than those for stimulated Brillioun scattering (SBS), the case of SBS is examined.

The Brillouin gain can be characterized as transient or steady state, depending on how the pump pulse compares to the phonon lifetime. Transient gains are much lower than steady-state gains. The steady-state case will be examined first. The steady-state gain coefficient at 1064 nm for backward SBS in pure water is measured to be 3.8 cm/GW.[29] Correcting the gain coefficient by $\cos(\pi/4)$ to the transverse scattering gain yields a transverse SBS gain coefficient at 1064 nm of 2.7 cm/GW. The maximum output-beam intensity is taken to be 4 GW/cm^2 external to the amplifier. In the amplifier the intensity is reduced by the factor of the refractive index due to the Brewster's angle input. Accounting for the average 1.38 refractive index of the cooling mixture, the pump intensity I_p is 2.8 GW/cm^2. Assuming a perfectly spatially flat output profile, the maximum transverse dimension L is then equal to the maximum width of the beam or 3.6 cm. The gI_pL product is then

$$gI_pL = 27. \tag{26}$$

A gI_pL product of 30 or more is generally accepted as being required for significant Stokes wave growth from noise. Note that this is a very conservative estimate because the pulse widths of interest here (~ few nanoseconds) are of the same order as the phonon lifetime for water, placing this problem clearly in the transient regime, where the SBS gains are much lower.

Table 68.V: The friction factor for various Reynolds numbers.

$f = \frac{64}{Re}$		Fully developed laminar flow
$f = 0.316\, Re^{-0.25}$; $Re < 2 \times 10^4$	}	Fully developed turbulent flow
$f = 0.184\, Re^{-0.25}$; $Re > 2 \times 10^4$		

Since the coolant is a mixture of ethylene glycol and water, the case of pure ethylene glycol is examined next. The measured transverse SBS gain coefficient for ethylene glycol at 532 nm is 0.60 cm/GW.[30] The measured transverse SBS gain coefficient for water at 532 nm is 2.1 cm/GW.[31] The gain coefficients for ethylene glycol at 532 nm is therefore ~0.3 that of water and, assuming similar wavelength scalings to 1054 nm, will be no worse a threat than SBS from water.

5. Mounting

The slab was mounted in the configuration shown in Fig. 68.45, which is a departure from the square edge used in numerous experimental test beds.[10,32] This geometry has mechanical, thermal, and optical advantages that combined provide significant performance improvements. The edges of the slab are pitch polished to an inspection finish with the glass and metal bonded by an air-cured silicone adhesive.[33]

The philosophy of the mounting configuration is to ensure minimum risk to the slab, should a debond in the silicone bonding layer occur. If a debonding in the silicon layer were to occur, the slab could move only in the *z*-direction. This configuration also removes the bulk of the adhesive from direct pump-light radiation.

The thermal benefits of the beveled slab are quite significant. The finite element program ANSYS[34] was used to solve both the thermal and stress distributions in the slab. Figure 68.46 shows the temperature distribution of a uniformly loaded, square-edged slab with the edge of the slab as a perfect insulator. As one would expect, the temperature distribution is uniform. Figure 68.47 shows a slab with bevels added. Notice the isotherms turn up so that they terminate normal to the slab boundary, once again as expected. This implies that a perfect insulator is not required at the slab boundary. Figure 68.48 shows the uniformly loaded slab with the silicon adhesive and metal frame added. Notice the change in the isotherms due to conduction at the edge. Figure 68.49 shows the resultant temperature distribution when the slab is loaded with the pump profile predicted by ZAP. As can be seen in Fig. 68.49, the thermal gradients occur in less than the St. Venant's region (one slab thickness).

Experimental

1. Gain and Gain Uniformity

Small-signal-gain experiments were performed in the center of the clear aperture using the ratio-of-ratios technique. This technique accounts for transmission losses; therefore, the gain values are gross gain. Figure 68.50 shows the con-

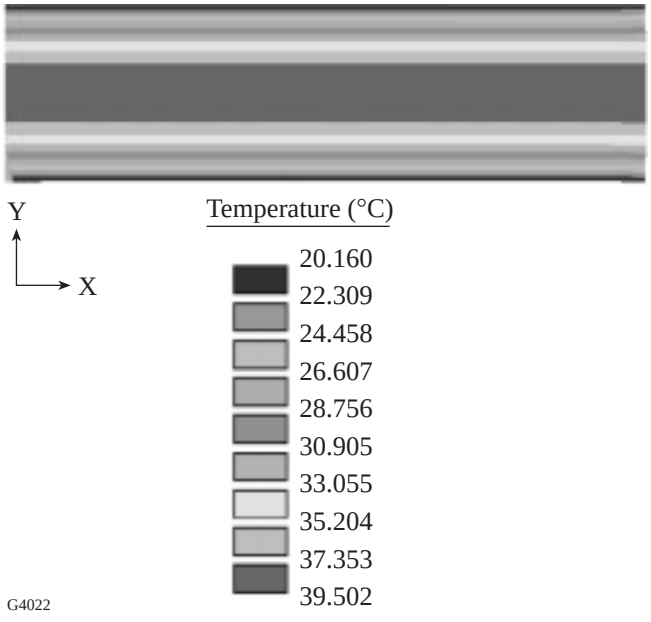

Figure 68.46
Steady-state isotherm plot of a uniformly loaded slab with square edges. The edges are treated as an adiabatic boundary.

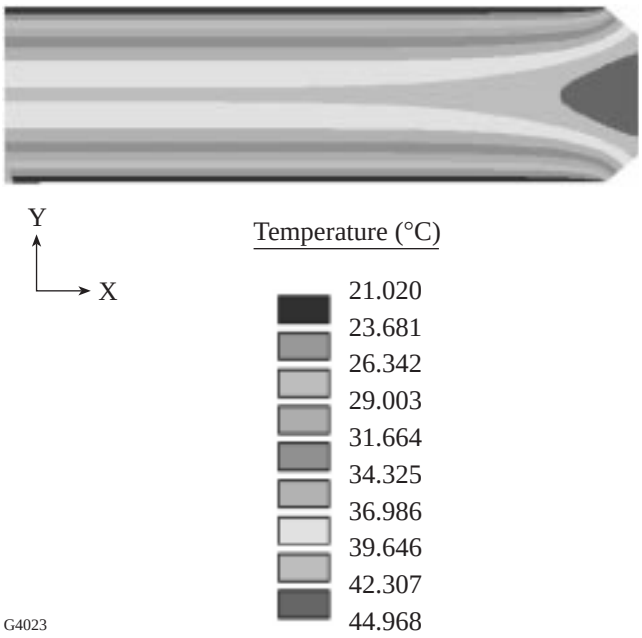

Figure 68.47
Steady-state isotherm plot of a uniformly loaded slab with beveled edges. The edges are treated as an adiabatic boundary.

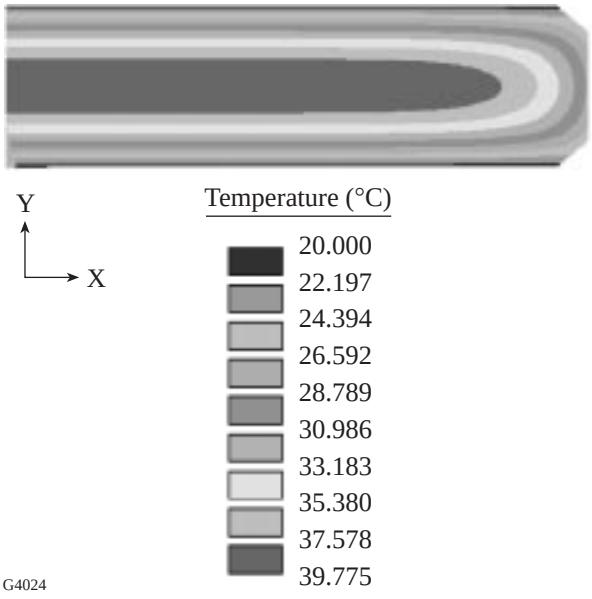

Figure 68.48
Steady-state isotherm plot of a uniformly loaded slab with beveled edges. The silicon bonding layer and stainless steel frame have been added as detailed in Fig. 68.43.

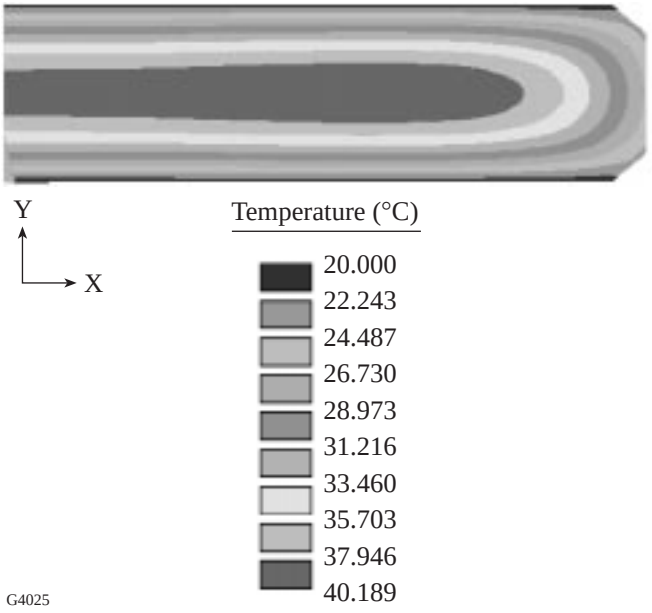

Figure 68.49
Steady-state isotherm plot of a slab loaded with a predicted pump profile. The silicon bonding layer and stainless steel frame have been added as detailed in Fig. 68.43.

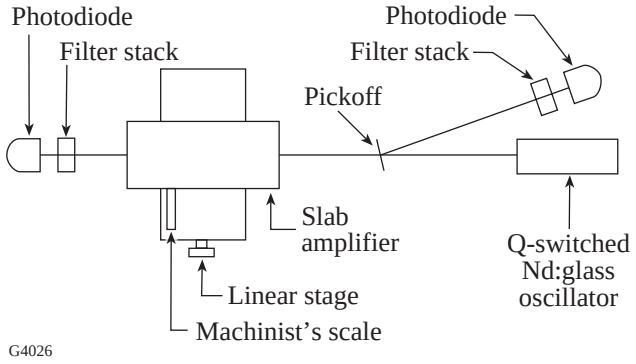

Figure 68.50
Experimental setup used for small-signal-gain and gain-mapping experiments.

figuration of the gain setup. The probe oscillator is a *Q*-switched Nd:glass oscillator that produces 100-ns FWHM pulses at 1054 nm. The reference and gain signals are detected using large-area photodiodes[35] to ensure that the entire probe beam is detected. Three sets of gain data were obtained, each of which corresponds to a different reflector type. The reflector types will be denoted as specular, metal diffuse, and ceramic diffuse.

The initial data runs were done as a function of bank energy. This data is shown in Fig. 68.51 for the two reflector types. As can be seen from the data, there is no parasitic clamping or ASE roll-off. Also from Fig. 68.51, it is observed that there is no performance penalty for using diffuse reflectors. The storage efficiency is plotted in Fig. 68.52 as a function of stored energy in the slab. This clearly shows characteristic roll-off in efficiency with increasing stored energy.

Mounting the amplifier on a linear stage allows gain mapping across the aperture. For all reflector types, the gain map was obtained with the probe beam (2-mm diameter) centered vertically in the clear aperture. Data points were obtained every 0.1 in. across the physical aperture. For the specular reflectors, the gain mapping was performed at three different bank energies. The three bank energies cover the anticipated operating range of the amplifier. Figure 68.53 shows the resultant normalized data compared to a predicted pumping profile. From Fig. 68.53, a pump uniformity of ±6% is observed. Two conclusions can be drawn from this data: (1) the pump profile was independent of the 4- to 7-kJ bank-energy range, and (2) agreement between predicted and experimental values was within the error bars of the code.

Normalized data for the diffuse reflectors is shown in Fig. 68.54 along with the corresponding predicted profile. Data for the diffuse reflectors was obtained at only the bank energy for which the slab was designed. The data was normalized to

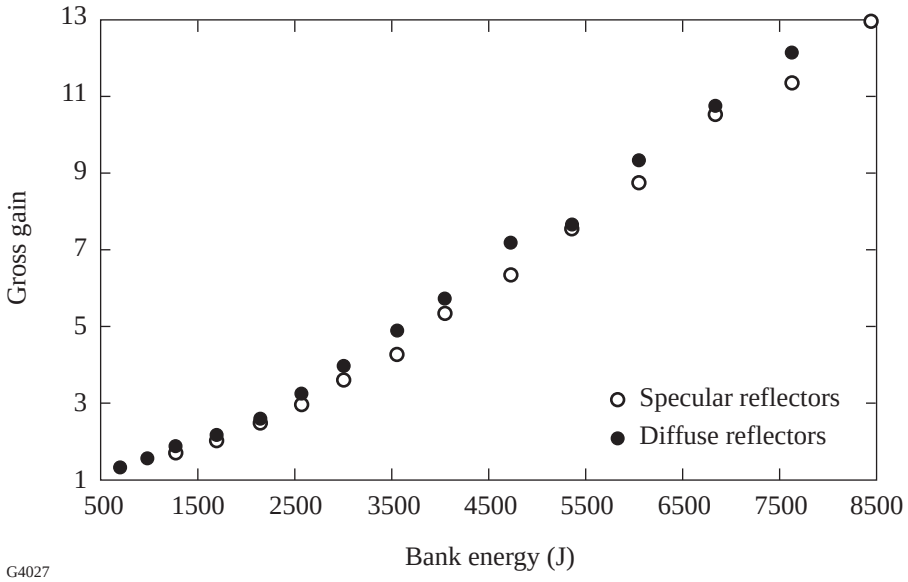

Figure 68.51
Plot of gross gain as a function of bank energy for both specular and diffuse reflectors.

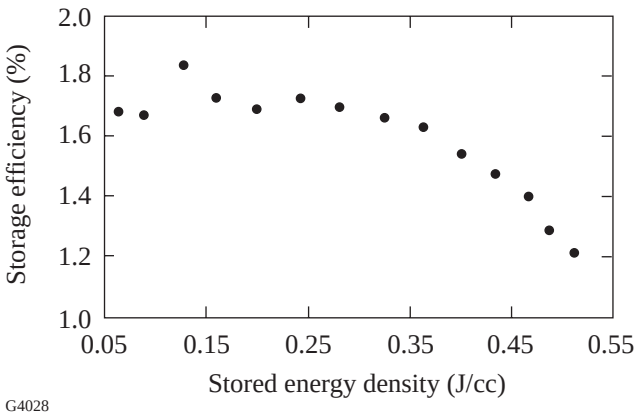

Figure 68.52
Storage efficiency as a function of stored energy in the slab.

the average stored energy across the slab aperture. There is virtually no difference between the two sets of reflectors. From Fig. 68.54, a pump uniformity of ±3% is observed. This is important since it gives us a method of producing inexpensive and effective reflectors.

2. Birefringence Mapping

Birefringence maps for all reflector types were obtained using the setup shown in Fig. 68.55. The laser source was a diode-pumped Nd:YAG.[36] Due to the stability of the laser, no reference signal was needed. The polarizer analyzer pair was chosen such that a contrast ratio of 2500:1 could be obtained. The intensity of the probe laser was then measured with the polarizers both crossed and uncrossed. For data with uncrossed polarizers, a set of calibrated optical density filters[37] were

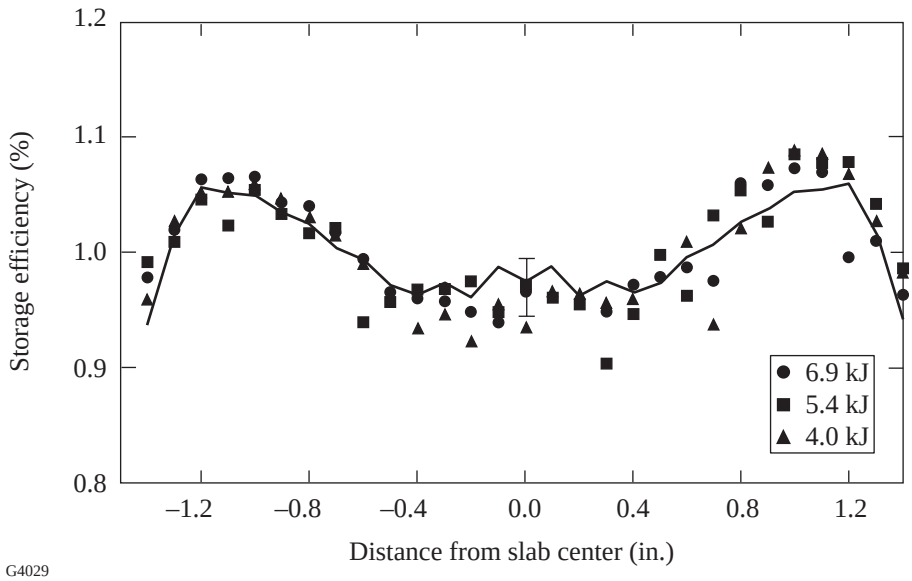

Figure 68.53
Normalized-stored-energy map for specular reflectors at three discrete bank energies. Also shown is the predicted pump profile with 3σ error bars.

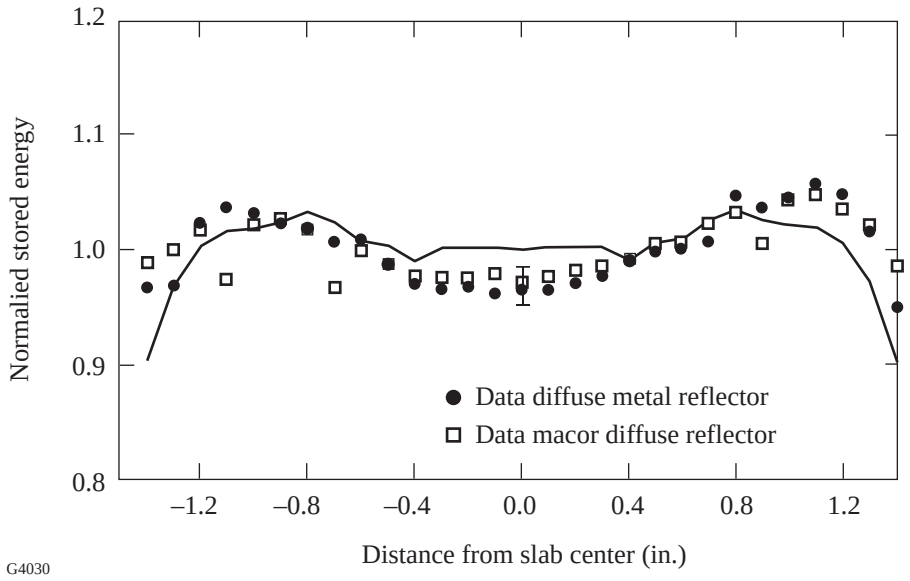

Figure 68.54
Normalized-stored-energy map for two different diffuse reflectors at the design bank energy. Also shown is the predicted pump profile with 3σ error bars.

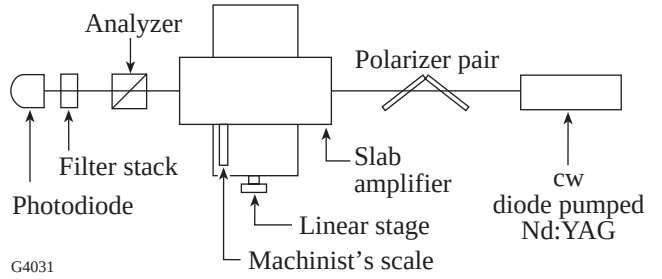

Figure 68.55
Experimental setup used for birefringence mapping.

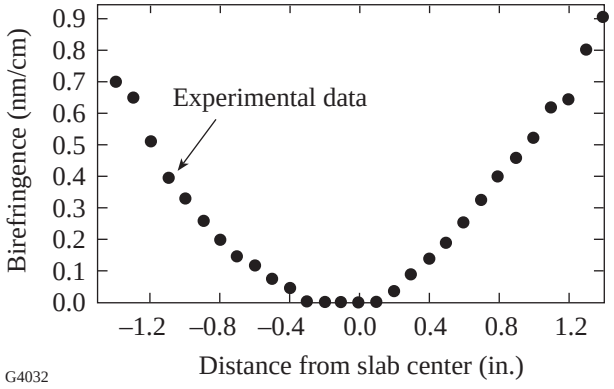

Figure 68.56
Steady-state birefringence map.

used to keep the signal on the diode below 1 V. This was done to maintain operation of the diode well within the linear range. Measurements with the polarizer analyzer pair crossed and uncrossed were obtained at 0.1-in. increments across the physical aperture.

The first depolarization data was obtained with the amplifier unpumped to measure any residual stress depolarization due to mounting and the glass itself. The remaining data was taken at 1 Hz at the designed bank energy. Figure 68.56 shows depolarization as a function of aperture for both reflector types.

3. Wavefront Evaluation

The wavefront of the slab was evaluated with the amplifier in one leg of a Mach-Zehnder interferometer (Fig. 68.57). The interferometric data was evaluated using spatial synchronous phase detection (SSPD).[38] This technique was developed by Takeda *et al.* with acquisition and analysis developed at LLE.[39] The probe source was a 1064-nm, *Q*-switched, cw source. The amplifier was run at 1 Hz at the design bank energy with the diffuse reflectors for at least 1 min prior to data acquisition to ensure that steady state had been achieved. This was verified to be a sufficient length of time by acquiring a second interferogram after 5 min of operation. Since we are interested in the steady-state effects and not the transient effects, data was collected between amplifier shots. Three sets of interferometric data were taken. The initial data was taken with the amplifier static; this served as the reference wavefront for which all subsequent data will be used. Next the coolant was turned on, which allowed us to measure directly the pressure-induced deformation of the Brewster windows. Finally the slab was pumped, which allowed us to measure the thermally induced wavefront deformation.

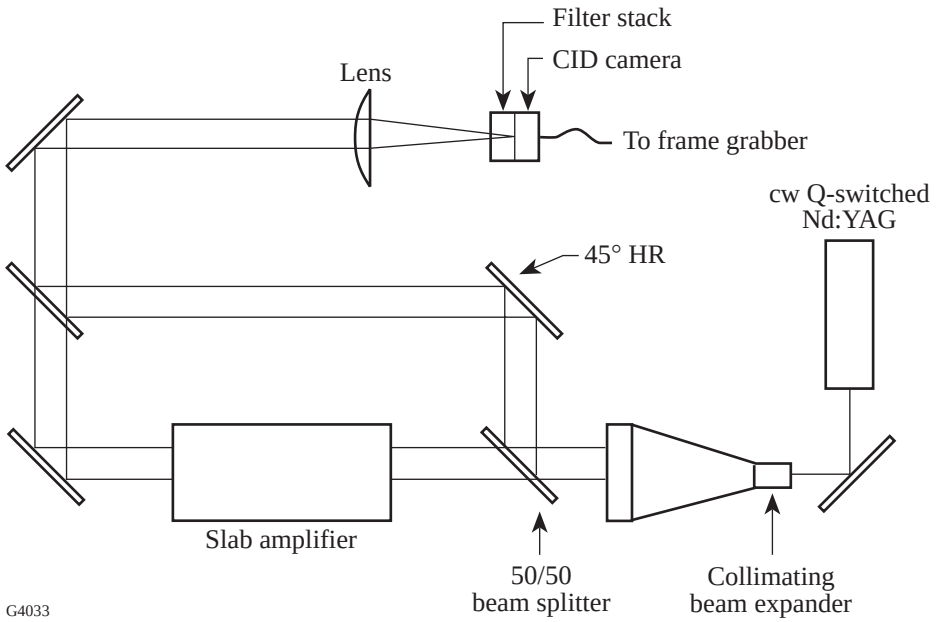

Figure 68.57
Mach-Zehnder interferometer setup for wavefront evaluation.

Figure 68.58 shows the pressure-induced wavefront with the static wavefront subtracted out. This compares with the previously predicted error. This effect can be reduced by (1) increasing the thickness of the Brewster windows, and (2) reducing the internal pressure in the slab by increasing the size of the coolant return lines.

Figure 68.59 shows the thermally induced wavefront error with the pressure-induced wavefront error subtracted out. Due to the very high fringe frequency at the edges of the physical aperture, data could not be extracted; however, data within the clear aperture was undisturbed. This effect is directly attributed to SSPD, which is primarily used for high-resolution

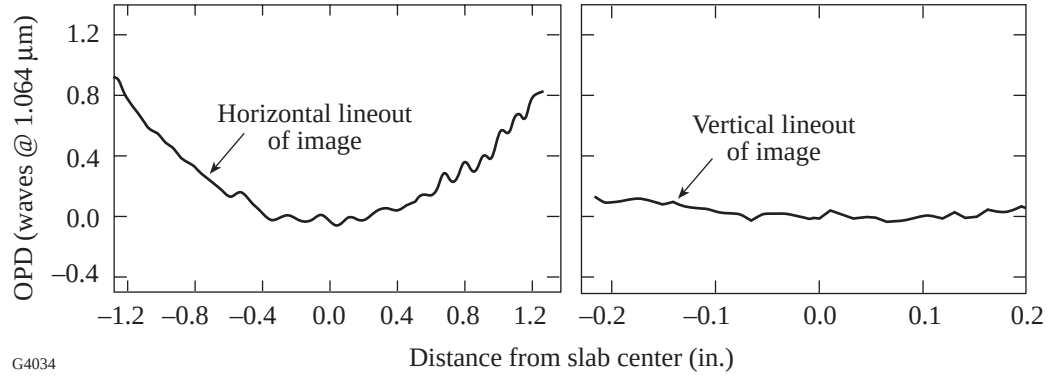

Figure 68.58
Pressure-induced wavefront error within the clear aperture.

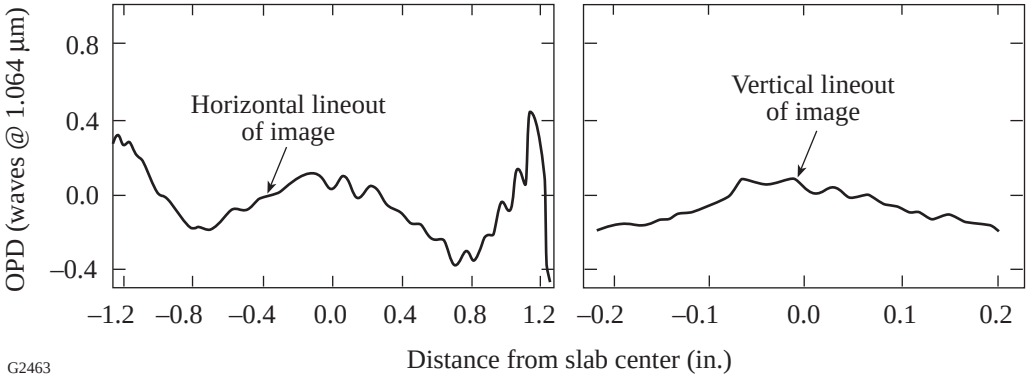

Figure 68.59
Thermally induced wavefront error within the clear aperture.

(λ/400) and is not well suited for multiple waves of deformation. The wavefront error bears a strong resemblance to the pumping profile, and it is natural to ask how much of the wavefront error is due to deformations of the pump faces of the slab. Using the measured pump profile, ANSYS was rerun to determine if indeed there is a connection.

4. System Performance

The slab was installed in LLE's damage test laser (DTL) (Fig. 68.60). This system has been used for materials testing and nonlinear optics experiments. The front end of the system consists of a 3-m, *Q*-switched, mode-locked Nd:phosphate glass oscillator running between 0.1 and 1.1 ns. Nominal operation of the system is at 0.8 ns. A single, 1-mJ pulse is amplified by a 1/4-in. × 6-in. Nd:glass rod capable of delivering up to 100 mJ of drive to the slab. The beam undergoes one-dimensional expansion in a Littrow prism anamorphic beam expander. The beam then passes through a 2× Galilean telescope before being injected into the slab. The pulse is then amplified with three passes through the slab. The output pulse is then spatially filtered before being converted to 527 nm or 351 nm. The frequency-conversion cell consists of KD*P, set up in a Type-II polarization mismatch scheme.[40]

Conversion-efficiency measurements were performed at the second and third harmonics. The results are shown in Table 68.VI; note that the peak conversion efficiency may not coincide with the peak energy due to conversion crystals of less than optimum thickness. The high conversion efficiency will allow for large-area materials testing at 351 nm.

Table 68.VI: System Performance

Wavelength	Conversion Efficiency	Energy
1054 nm	--	2.1 J
532 nm	68%	1.4 J
351 nm	55%	0.88 J

Summary

We successfully designed, constructed, and tested a large-aperture, high-gain, Nd:glass slab amplifier with a 2-Hz repetition rate. The slab was designed for a gross small-signal, single-pass gain of 8, although a maximum gross small-signal gain of 13 was obtained. These stored-energy densities were obtained without special ASE (amplified spontaneous emission) suppressors and with a pump uniformity of ±3%. This pump uniformity was achieved with a simple box reflector with diffusely reflecting surfaces. Two methods of producing this diffuse surface were found to give comparable pump profiles. This high degree of pump uniformity helped to minimize thermally induced wavefront errors that were less than 0.5 waves at 1054 nm in the clear aperture.

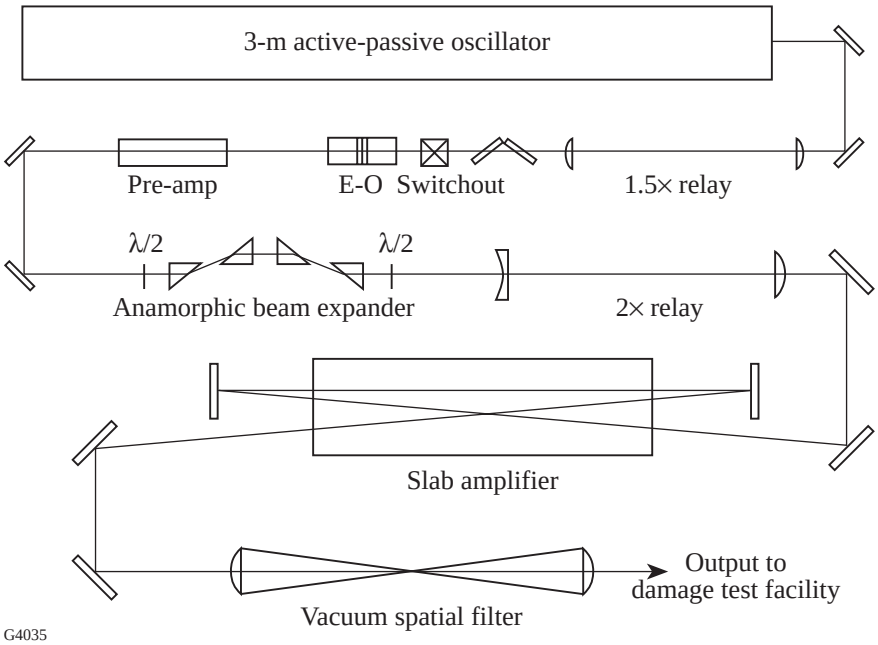

Figure 68.60
Damage test laser schematic.

When installed in LLE's damage test laser, the slab amplifier brought the system performance to the multijoule level with as little as 10 mJ of drive. This system has sufficient beam quality to permit high conversion efficiencies at the second and third harmonics.

ACKNOWLEDGMENT

The authors wish to thank the tool makers at JASCO Precision for the excellent fabrication of this amplifier. Thanks also to Steve Swales of LLE's Wavefront Analysis Laboratory for reducing the interferometric data. This work was supported by the U.S. Department of Energy Office of Inertial Confinement Fusion under Cooperative Agreement No. DE-FC03-92SF19460, the University of Rochester, and the New York State Energy Research and Development Authority. The support of DOE does not constitute an endorsement by DOE of the views expressed in this article.

REFERENCES

1. J. P. Chernoch and S. W. Martin, U. S. Patent No. 3,633,126 (17 April 1969).
2. R. L. Byer, presented at the International Lasers and Electro-Optic Exhibition, Tokyo, Japan, 26 January 1985.
3. R. L. Byer, Lawrence Livermore National Laboratory Report UCRL-15561 (1982).
4. J. M. Eggleston *et al.*, IEEE J. Quantum Electron. **QE-20**, 289 (1984).
5. T. J. Kane, J. M. Eggleston, and R. L. Byer, IEEE J. Quantum Electron. **QE-21**, 1195 (1985).
6. J. M. Eggleston *et al.*, IEEE J. Quantum Electron. **22**, 2092 (1986).
7. The largest body of work was described at the LLNL Medium-Average Power Conferences. Compendia of that work appear in the Lawrence Livermore National Laboratory Laser Program Annual Reports 1985–1987.
8. Product of Hoya Optics, Inc., 3400 Edison Way, Fremont, CA 94538. Use of a particular product does indicate endorsement by the University of Rochester.
9. D. C. Brown, in *High-Peak-Power Nd:Glass Laser Systems*, Springer Series in Optical Sciences, edited by D. L. MacAdam (Springer-Verlag, Berlin, 1981), Vol. 25, p. 45.
10. J. H. Kelly, D. C. Brown, J. A. Abate, and K. Teegarden, Appl. Opt. **20**, 1595 (1981).
11. M. J. Minot, J. Opt. Soc. Am. **66**, 515 (1976).
12. L. M. Cook *et al.*, Appl. Opt. **21**, 1482 (1982).
13. W. W. Simmons and W. E. Warren, in *Modeling and Simulation of Optoelectronic Systems*, edited by J. D. O'Keefe (SPIE, Bellingham, WA, 1986), Vol. 642, p. 166. Available as a Lawrence Livermore National Laboratory Report UCRL-94380 (1986).
14. This is conservative. Preferential deposition of energy near the slab faces due to Beer's law absorption helps the thermal loading problem. See J. B. Trenholme, Lawrence Livermore National Laboratory Laser Program Annual Report 1982, UCRL-50021-82 (1983), p. 7-112.
15. W. F. Krupke *et al.*, J. Opt. Soc. Am. B **3**, 102 (1986).
16. M. S. Mangir and D. A. Rockwell, IEEE J. Quantum Electron. **QE-22**, 574 (1986).
17. J. Rinefierd, S. D. Jacobs, D. Brown, J. Abate, O. Lewis, and H. Applebaum, Laboratory for Laser Energetics Report No. 82, 1978 (unpublished).
18. W. F. Hagen and M. O. Riley, Lawrence Livermore National Laboratory Laser Program Annual Report 1985, UCRL-50021-85 (1986), p. 9-69.
19. M. A. Summers, Medium Average Power Solid State Laser Technical Information Seminar, Lawrence Livermore National Laboratory, Livermore, CA, 4 November 1988.
20. Hoya Optics Inc. product literature, 3400 Edison Way, Fremont, CA 94538.
21. The code used here is an upgraded version of the ZAP Laser Analysis Program written by J. H. Alexander, M. Froost, and J. E. Welch, ARPA Order No. 660, Contract No. N00014-70-C-0341 (June 1971).
22. A. C. Erlandson, Lawrence Livermore National Laboratory Laser Program Annual Report 1985, UCRL 50021-85 (1986), p. 7-20.
23. Technical Bulletin 2, ILC Technology, 399 Java Drive, Sunnyvale, CA 94089.
24. Product of Corning Glass Works, Corning, NY 14831.
25. J. H. Kelly, D. L. Smith, J.-C. Lee, S. D. Jacobs, M. J. Shoup, III, and D. J. Smith, in *Conference on Lasers and Electro-Optics*, Vol. 7, 1988 OSA Technical Digest Series (Optical Society of America, Washington, DC, 1988), p. 380.
26. W. M. Kays and M. E. Crawford, *Convective Heat and Mass Transfer*, 2nd ed. (McGraw-Hill, New York, 1980).
27. F. P. Incropera and D. P. Dewitt, *Fundamentals of Heat and Mass Transfer* (Wiley, New York, 1985).
28. J. M. Eggleston and M. J. Kushner, Opt. Lett. **12**, 410 (1987).
29. J. F. Reintjes, "Stimulated Raman and Brillouin Scattering," in *CRC Handbook of Laser Science and Technology*, Supplement 2: Optical Materials, edited by M. J. Weber (CRC Press, Boca Raton, FL, 1995), Sec. 8, p. 358, Table 8.3.7.
30. These numbers were taken from Ref. 29 and corrected by the factor $\cos(\pi/4)$ to obtain the transverse gain.
31. W. Kaiser and M. Maier, in *Laser Handbook*, edited by F. T. Arecchi and E. O. Schulz-Dubois (North-Holland, Amsterdam, 1972), Vol. 2, p. 1077.
32. J. M. Eggleston *et al.*, Opt. Lett. **7**, 405 (1982).
33. Product of General Electric Company, Silicon Products Division, Naperville, IL 60540.

34. G. J. DeSalvo and J. A. Swanson, Swanson Analysis Systems, Inc. (1 June 1985). (ANSYS is a registered trademark of Swanson Analysis Systems, Inc., Johnson Road, Houston, PA 15342).

35. Product of United Detector Technologies, 12525 Chadron Avenue, Hawthorne, CA 90250.

36. Product of Amoco Laser Company, 1251 Frontenac Road, Naperville, IL 60540.

37. Product of Schott Technologies, Inc., 400 York Avenue, Duryea, PA 18462.

38. M. Takeda, H. Ina, and S. Kobayashi, J. Opt. Soc. Am **72**, 156 (1982).

39. Laboratory for Laser Energetics LLE Review **31**, NTIS document No. DOE/DP/40200-47, 1987 (unpublished), p. 114.

40. R. S. Craxton, IEEE J. Quantum Electron. **QE-17**, 1771 (1981).